

Instanton contributions to the low-lying hadron mass spectrum

Samuel D. Thomas, Waseem Kamleh, and Derek B. Leinweber
*Special Research Centre for the Subatomic Structure of Matter (CSSM),
 School of Chemistry and Physics, University of Adelaide, South Australia 5005, Australia*
 (Dated: September 24, 2015)

The role of instanton-like objects in the QCD vacuum on the mass spectrum of low-lying light hadrons is explored in lattice QCD. Using over-improved stout-link smearing, tuned to preserve instanton-like objects in the QCD vacuum, the evolution of the mass spectrum under smearing is examined. The calculation is performed using a $20^3 \times 40$ dynamical fat-link-irrelevant-clover (FLIC) fermion action ensemble with lattice spacing 0.126 fm. Through the consideration of a range of pion masses, the effect of the vacuum instanton content is compared at a common pion mass. While the qualitative features of ground-state hadrons are preserved on instanton-dominated configurations, the excitation spectrum experiences significant changes. The underlying physics revealed shows little similarity to the direct-instanton interaction predictions of the instanton liquid model.

I. INTRODUCTION

The instanton [1] is well known as a classical solution to the pure-gauge Yang-Mills equations. It has topological change ± 1 , action $8\pi^2/g^2$, and is associated with a localised zero eigenmode of the Dirac operator. Various models exist for the QCD vacuum as composed purely of superpositions of these objects and here we consider the random instanton liquid model (RILM) [2–7] as a point of comparison. Phenomenology constrains the RILM model parameters including $\rho_{\text{inst}} \approx 0.33$ fm for the average instanton size and $n \approx 1$ fm $^{-4}$ for the pseudo-particle density.

Such a model vacuum generates approximate Dirac zero-modes with definite chirality. A quark propagating via a zero-mode changes its chirality. Thus, the masses of the pseudoscalar channels (the pion, and the diquark in the nucleon) have direct instanton-induced contributions which are attractive and reduce their mass. By comparison, the rho as a vector meson has instanton contributions only at a higher level (analogous to a 2π intermediate state). Similarly, the Delta has interactions only at the 6-pseudoparticle level and higher [8–12].

We wish to determine what role the instantons present in the QCD vacuum of lattice QCD simulations play in the determination of hadron phenomenology. Starting from a Monte-Carlo generated calculation of QCD on the lattice, we filter out the short-distance gluonic interactions such that the underlying instanton degrees of freedom are revealed. We use over-improved stout-link smearing [13] to do this and the merits of this approach are discussed in Sec. II.

Section III provides an overview of the lattice QCD simulation methods and associated parameters. It also describes our correlation matrix approach which enables us to accurately determine both the ground-state hadron spectrum and the first radial excitations.

We will then examine the low-lying hadron spectrum as a function of smearing in Sec. IV, monitoring its evolution as the QCD vacuum progresses from having significant topological structure, most of it not instanton-like, through to being both instanton-dominated and eventually sparse as nearby instanton-anti-instanton pairs annihilate. Conclusions are drawn in Sec. V.

II. REVEALING INSTANTONS

Early methods of smoothing short-distance fluctuations to reveal the underlying instanton degrees of freedom used cooling. This proceeds by replacing each link $U_\mu(x)$ on the lattice by a new link such that the gluonic action is minimised. Unfortunately, this approach also tends to remove the topological configurations of interest from the lattice. This occurs due to the discretisation error involved in minimizing the local action. Expanding the gluonic Wilson action in terms of a single-instanton solution one finds [14]

$$S_{\text{inst}} = \frac{8\pi^2}{g^2} \left\{ 1 - \frac{1}{5} \left(\frac{a}{\rho} \right)^2 + O(a^4) \right\}. \quad (1)$$

Thus the discretisation error enables one to reduce the action by reducing the instanton size parameter ρ . Upon minimizing the action, instantons shrink. At sufficient cooling, they will become small enough that significant discretisation errors will allow them to ‘fall through’ the lattice.

It is possible, however, to include larger combinations of loops having different discretisation errors. Coefficients can be chosen such that the $O(a^2)$ error is cancelled [15], giving the ‘improved’ action. Unfortunately this method still leads to a negative leading $O(a^4)$ discretisation error, and the same unwanted corrosion of topological objects. Higher order terms composed from combinations of larger loops can also be included in the action, but this requires increasing accuracy on the perturbative corrections to the improvement coefficients, typically estimated via the mean link of tadpole improvement.

Instead, one can adopt the approach of over-improvement [13, 14] and express the action in terms of an improvement parameter ϵ ,

$$S(\epsilon) = \beta \sum_x \sum_{\mu > \nu} \left\{ \frac{5 - 2\epsilon}{3} (1 - P_{\mu\nu}(x)) - \frac{1 - \epsilon}{12} [(1 - R_{\mu\nu}(x)) + (1 - R_{\nu\mu}(x))] \right\}, \quad (2)$$

where $P_{\mu\nu}(x)$ denotes 1/3 of the real trace of the clover average of the four plaquettes touching the point x and similarly $R_{\mu\nu}(x)$ denotes 1/3 of the real trace of the clover av-

erage of four 2×1 Wilson loops. The choice of 2×1 rectangles over the 2×2 squares in Ref. [13] is in the interest of preserving locality and minimizing the number of links. The coefficients are chosen such that $\epsilon = 1$ gives the unimproved Wilson action and $\epsilon = 0$ provides an $O(a^2)$ -improved action. We can also compare the behavior of the smearing algorithm to that provided by the Wilson or gradient flow, as in Ref. [16]. For $\epsilon = 0$, N sweeps of stout-link smearing is equivalent to $t = \alpha N$ for the Wilson flow time as long as the smearing parameter α is sufficiently small. We use $\alpha = 0.06$ which is even smaller than the standard $\alpha = 0.1$ for stout-link smearing.

A negative value for the ϵ parameter will lead to a positive leading-order discretisation error which inhibits the shrinking of instanton-like structures under smearing. However a large negative value would cause instantons to grow under smearing. We use an ϵ value of -0.25 , as recommended in Ref. [13] providing the required stability with marginal discretisation error. The effect of ϵ is also studied in Sec. IV.

This scheme preserves instanton-like objects with a size parameter ρ greater than the dislocation threshold of $1.97 a$ [13]. Herein, $a = 0.126$ fm such that instantons of size $\rho < 0.25$ fm will be removed under over-improved stout-link smearing [13]. However, this effect may be regarded as small. The scale dependence of the instanton action $S_0 = 8\pi^2/g^2$ on the coupling constant g in the context of asymptotic freedom suppresses the presence of small instantons. A study of the instanton distribution within dynamical gauge fields with light dynamical quarks provides [17] $\rho_{\text{inst}} = 0.415$ fm with the standard deviation of the distribution of instanton sizes of only 0.075 fm indicating a sharply peaked distribution with few small-size instantons.

An additional effect of smearing is that any smearing algorithm designed to suppress short-distance perturbative interactions from the gauge field will also tend to annihilate closely spaced instanton–anti-instanton pairs. As the effect of this is mainly to reduce the pseudo-particle density, we expect a corresponding change in the quark condensate [4]. We will use this behaviour of the smearing algorithm to examine the lattice QCD vacuum as it progresses from having significant topological structure, most of it not instanton-like, through to being both instanton-dominated and sparse.

III. SIMULATION METHODS

A. Correlation Functions and the Variational Approach

The low-lying hadronic masses can be extracted from the lattice by analysis of their corresponding 2-point correlation functions. This correlation function is defined as $G_2(x) = \langle 0 | \chi(x) \bar{\chi}(0) | 0 \rangle$, where χ is the interpolating field corresponding to the hadron of interest. The correlation function, in momentum space, is then of the form

$$G_2(\vec{p}, t) = \sum_{\vec{x}} \exp(-i\vec{p} \cdot \vec{x}) \langle 0 | \chi(x) \bar{\chi}(0) | 0 \rangle. \quad (3)$$

Inserting a complete set of states, $|B\rangle$, and utilising the translation operator, one obtains the Euclidean time correlator

$$G_2(\vec{p}, t) = \sum_B e^{-E_B(\vec{p})t} \lambda_B(\vec{p}) \bar{\lambda}_B(\vec{p}) \quad (4)$$

with $\lambda_B(\vec{p}) = \langle 0 | \chi | B, \vec{p} \rangle$ describing the coupling of the state B with momentum \vec{p} to the operator χ and $E_B(\vec{p})$ the on-shell energy of the state.

The determination of the mass of the lowest lying state is hampered by the tower of exponentials from excited state contributions. Although these are suppressed by the factor $e^{-E_B t}$, it is often difficult to wait until a sufficiently large Euclidean time where all excited state contaminations have vanished. Moreover, with broad fermion source smearings and narrow fermion sink smearings, excited states can enter with a negative weight and create false plateaus.

This problem is particularly challenging on smeared configurations. As we will see, hadronic excited states do not maintain a significant mass splitting from the ground-state hadrons making the extraction of even the ground-state mass difficult.

The solution to the state isolation problem is now well established. One considers a matrix of correlation functions in a variational analysis [18–20]. The operators used to create the correlation functions can be chosen to have any form (as long as they have the correct quantum numbers). Different operators have different couplings λ_B to each state, B and one seeks linear combinations of the operators constructed to isolate each state of the spectrum.

The best approach for isolating a state within a tower of states excited by a particular interpolating field is to introduce differently sized covariantly smeared sources and sinks [21–23]. Physical hadrons are extended objects, and a linear combination of Gaussian sources allows one to approximate the hadronic wave function [24]. This allows for a precise determination of ground-state properties. The suppression of excited states provides ground-state isolation early in Euclidean time. The approach also provides access to the excited states having the same spin and parity.

We solve the generalized eigenvalue problem for the matrix G_{ij} whose elements are the correlation functions generated from the operators χ_i and $\bar{\chi}_j$, normalised at the fermionic source time. If $\bar{\phi}^\alpha = u_j^\alpha \bar{\chi}_j$ is an operator constructed to isolate state α , then the recurrence relation relating times t_0 and $t_0 + dt$

$$G_{ij}(t_0 + dt) u_j^\alpha = e^{-E_\alpha dt} G_{ij}(t_0) u_j^\alpha, \quad (5)$$

can be used to construct a generalised eigenvalue equation for the right eigenvector u^α and eigenvalue $e^{-E_\alpha dt}$

$$G^{-1}(t_0) G(t_0 + dt) u^\alpha = e^{-E_\alpha dt} u^\alpha. \quad (6)$$

The reference times t_0 and interval dt must be selected to lie within a region where the excited state contributions are strong and not yet exponentially suppressed. However, some amount of Euclidean time evolution is helpful in reducing the number of states contributing significantly in the correlators to the dimension of the correlation matrix such that state isolation is achieved.

While the eigenvalues of the generalised eigenvalue equations depend strongly on the values of these variational parameters, t_0 and dt , the associated eigenvectors are robust against this variation. A similar analysis can be done to obtain the left eigenvector v^α from which a state-projected correlator $v_i^\alpha G_{ij}(t) u_j^\alpha$ can be constructed.

This correlator is insensitive to the variational parameters. In practice, a t_0 value one or two time steps from the source accompanied by a dt value of two or three lattice time steps provides good eigenstate isolation in the projected correlator. One can then apply standard analysis techniques using the covariance matrix-based χ^2 per degree of freedom to carefully identify the Euclidean time regime dominated by a single eigenstate.

B. Simulation Methods and Parameters

Previous works in this vein [25–28] were considered in the mid to late 1990s. While they often considered the quenched approximation, a greater concern is the use of standard cooling algorithms based on the Wilson gauge action.

As discussed in Sec. II, this algorithm rapidly destroys the instanton-like topological structures that one is attempting to study. In this case, the final smeared configuration is much closer to a dilute instanton gas than to an instanton liquid.

The calculations presented herein are performed on an ensemble of 76 2-flavour $20^3 \times 40$ gauge field configurations generated using dynamical fat-link-irrelevant-clover (FLIC) fermions [29–33], with lattice coupling $\beta = 3.94$ and an $SU(3)$ -flavour symmetric hopping parameter $\kappa = 0.1324$, providing $m_\pi = 540$ MeV. The lattice spacing associated with the string tension is $a = 0.126$ fm, providing a spatial extent of 2.52 fm. As a smearing sweep is a local short-distance effect that does not affect the string tension, we consider the lattice spacing to be unaltered under a smearing sweep. Cumulative smearing sweeps do affect long-distance physics and we will examine this effect in the following section.

The smearing of the gauge field is performed using over-improved stout-link smearing [13] with $\epsilon = -0.25$ and an isotropic smearing parameter $\alpha_{sm} = 0.06$, smaller than the typical value [34] of 0.10.

Valence quark propagators are calculated via the FLIC fermion action at multiple κ values. The boundary conditions are periodic in the spatial dimensions, and fixed in the Euclidean time dimension. The fermionic source is inserted away from the boundary at $t = 10$, sufficient to avoid artifacts associated with the boundary. In constructing a basis for our variational approach to isolating states, we use gauge invariant Gaussian smeared [35] fermion sources. The smearing procedure is:

$$\psi_i(x, t) = \sum_{x'} F(x, x') \psi_{i-1}(x', t), \quad (7)$$

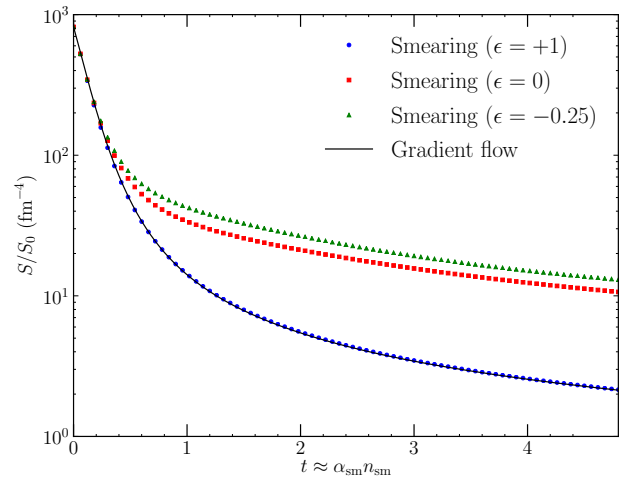


FIG. 1. The evolution of the action density for a typical configuration under various methods of smearing. $\epsilon = 1$ is the Wilson action, and $\epsilon = 0$ corresponds to the $\mathcal{O}(a^2)$ -improved action. The action under over-improved smearing ($\epsilon = -0.25$) lies above either of these as required. With the identification $t = \alpha_{sm} n_{sm}$, numerical integration of the Wilson flow agrees with smearing using the Wilson action. The highest level of smearing considered in the following sections (60 sweeps) is equivalent to a Wilson flow time of $t = 3.6$.

where

$$F(x, x') = (1 - \alpha) \delta_{x, x'} + \frac{\alpha}{6} \sum_{\mu=1}^3 [U_\mu(x) \delta_{x', x+\hat{\mu}} + U_\mu^\dagger(x - \hat{\mu}) \delta_{x', x-\hat{\mu}}], \quad (8)$$

and the parameter $\alpha = 0.7$ is used in our calculation. After repeating the procedure N_{sm} times on a point source the resulting smeared fermion field is,

$$\psi_{N_{sm}}(x, t) = \sum_{x'} F^{N_{sm}}(x, x') \psi_0(x', t). \quad (9)$$

We consider $N_{sm} = 10, 25, 50, 100$, and 150 sweeps in constructing effective correlation-matrix bases.

IV. RESULTS

A. Gluonic observables

We begin by examining the effect of stout-link smearing on the action of our gauge-field ensemble. Figure 1 displays the evolution of the action as a function of the number of smearing sweeps. For our choice of $\epsilon = -0.25$, after only 10 sweeps of smearing, the action has dropped to one tenth of its initial value. The majority of the short-distance interactions are removed within the first few iterations of smearing. It takes another 50 sweeps of smearing for the action to reduce by another order of magnitude. The Wilson flow is also shown

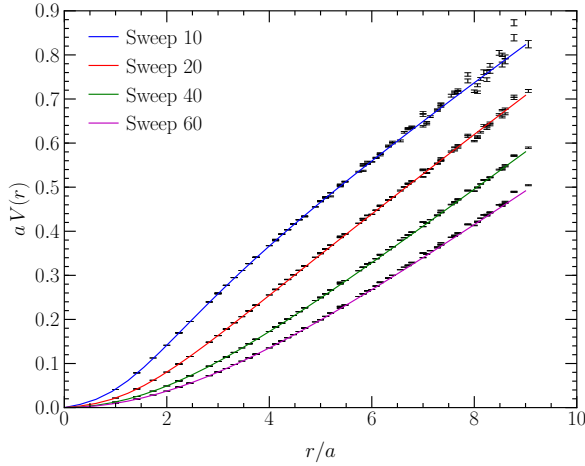


FIG. 2. The evolution of the static quark potential under various levels of over-improved stout-link smearing.

TABLE I. The best fit parameters for the Padé of Eq. (10) fit to the lattice QCD results for the static quark potential illustrated in Fig. 2. Uncertainties in the parameters are determined from a single-elimination jackknife analysis.

Sweep	a_1	a_2	a_3	b_0	b_1
10	0.093(2)	0.01(1)	0.082(1)	4.7(2)	-1.22(5)
20	0.062(1)	0.020(4)	0.084(1)	6.4(2)	0.22(3)
40	0.035(1)	0.212(4)	0.081(1)	21.4(3)	3.28(5)
60	0.02(5)	0.384(1)	0.073(1)	42(1)	5(1)

for comparison of smearing extent. We will focus on ensembles following 10, 20, 40, and 60 sweeps of smearing; these correspond to Wilson flow times of 0.6, 1.2, 2.4, and 3.6 respectively.

In Fig. 2, the static quark potential, determined from the Wilson loop, is shown for configurations at various levels of smearing. The attractive Coulomb-potential behavior at small r is lost rapidly under smearing as the algorithm removes short-distance interactions. The fit is a third-order Padé approximant constrained by the short-distance behaviour $V \rightarrow V_{free} = 0$ and the long-distance behaviour of a linearly rising potential. It has the form

$$V(r) = \frac{a_1 r + a_2 r^2 + a_3 r^3}{b_0 + b_1 r + r^2}. \quad (10)$$

The large r slope of the potential reflects the approximate invariance of the string tension and associated lattice spacing. Best fit parameters are summarised in Table I.

For sufficiently large r , the parameter a_3 is equivalent to the string tension σ and we note it remains almost constant under moderate levels of smearing. This differs significantly from the behavior reported in Ref. [25] where the string tension was reduced to only 27% of its original value after 25 sweeps of the unimproved cooling algorithm. This also differs from the theoretical prediction of the instanton liquid model, which

was shown to generate a string tension [36], but with a value much smaller than the physical value. The over-improved stout-link smearing algorithm tuned specifically to preserve instanton-like structure in the gauge field configurations retains the long-distance string tension remarkably well.

The process of stout-link smearing is expected to remove the short distance physics up to an effective radius [37] which may be parameterised as

$$R = a (c \rho_{sm} N_{sw})^{1/2}, \quad (11)$$

under the random-walk hypothesis. The coefficient c is a proportionality constant determined [37] to be $c = 6.15(3)$. The smearing radii for our selected values of $N_{sw} = 0, 10, 20, 40, 60$ are $R/a = 0, 1.9, 2.7, 3.8$, and 4.7 respectively. While this explains the preservation of the string tension observed in Fig. 2 and Table I, one needs to examine the extent to which an ensemble of instantons has been isolated in the QCD vacuum.

The instanton content of the vacuum under the same over-improved stout-link smearing algorithm selected herein was also studied in Ref. [38]. To examine the extent to which the non-trivial topology identified on the lattice is consistent with instantons, two measures of the local maxima of the action density found on representative configurations were measured and compared to the classical instanton solution. The instanton size is measured by fitting the profile of the action density in a $(2a)^4$ hypercube surrounding the position of the local maximum to the classical instanton action density

$$S_0(x) = \xi \frac{6}{\pi^2} \frac{\rho^4}{((x - x_0)^2 + \rho^2)^4}. \quad (12)$$

Here ξ , ρ and x_0 are fit parameters, noting that x_0 is not restricted to a lattice site. The parameter ξ is introduced as lattice topological objects often have a higher action than classical instantons. We wish to determine the size, ρ , by using the shape of the action density around the local maximum, rather than the height. Considering the relative RMS deviation over the 3^4 hypercube of points surrounding the local maximum, $\sqrt{\frac{1}{V-1} \sum_{x \in V} (S_0(x) - S(x))^2 / S_0}$, we find (Eq. 12) fits the data with a typical percentage deviation of 10%. This deviation decreases as the gauge fields are smeared.

We can then compare the size of instanton candidates to the value of the topological charge at the centre of an (anti-) instanton in the context of the classical instanton relationship

$$q(x_0) = Q \frac{6}{\pi^2 \rho^4}, \quad (13)$$

where $Q = \mp 1$ for an (anti-)instanton. $q(x_0)$ at the fitted values of x_0 are found using linear interpolation from neighbouring hypercubes to find an extremum inside the hypercube containing x_0 .

Fig. 3, reproduced from Ref. [38], displays the values found on a smoothed lattice at various smearing levels and compares the distribution with the classical relationship of Eq. (13), illustrated by the curves. The degree to which fitted results concur with Eq. (13) provides insight into the extent to which the

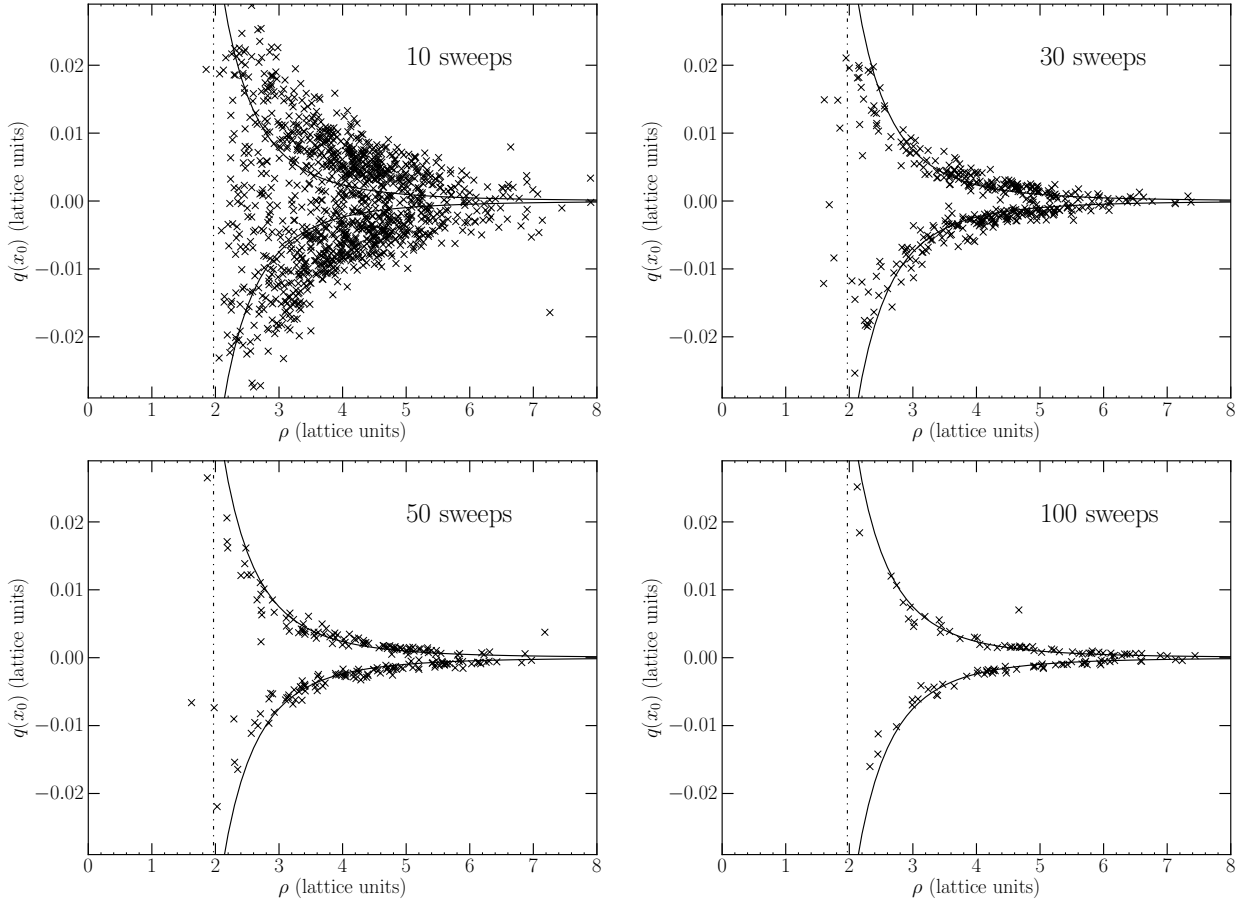


FIG. 3. Instanton content of a single representative gauge field configuration under the over-improved stout-link smearing algorithm at 10, 30, 50 and 100 sweeps of smearing; reproduced using data from Ref. [38]. At each smearing level, the gauge action $S/S_0 = 2099, 445, 252, 130$; topological charge $Q = -9.45, -7.36, -6.38, -6.02$, and approximate instanton number (determined only by the number of candidates) $n = 1222, 400, 214, 116$. The values of the instanton size, ρ , found by fitting lattice maxima of the action to the classical instanton action density are plotted as crosses, against the topological charge at the centre, $q(x_0)$. The results are compared to the theoretical relationship between the instanton radius and topological charge at the centre (solid lines), and the dislocation threshold of the algorithm, $1.97a$ (dash-dotted line). The pseudoparticle densities underlying the gauge fields considered remain higher than the phenomenologically assumed value of $\approx 1 \text{ fm}^{-4}$, which would correspond to an instanton number of ≈ 80 .

topology of the gluon fields resembles an ensemble of instantons.

At low levels of smearing we expect to fit a large number of local maxima which are not associated with the nontrivial topology of instantons; local maxima of the action corresponding to noise. At 10 sweeps, the number of instanton candidates is large and distributed with sizes greater than the dislocation threshold of ~ 2 through 8 lattice units. There is little correlation to the predicted charge lines of Eq. (13). However, this quickly changes as the number of smearing sweeps increases, eventually leading to a very close approximation to Eq. (13). In this case the distribution reflects an ensemble of topological objects approximating classical instanton solutions. In principle, there are also classical solutions with non-trivial holonomy (i.e. calorons) which wrap around the temporal extent of the lattice. In these cases we would not expect the same relationship between the topological charge and

action densities. Such objects would be revealed by an unusually poor or nonconvergent fit to the action density (Eq. 12) or by lying far from the expected relationship curve (Eq. 13, Fig. 3.) The number of instanton candidates steadily decreases with smearing through the process of neighboring instanton–anti-instanton annihilation. By 100 sweeps the number of instanton candidates has been thinned to the point that they are usually well-separated and thus the annihilation of instanton pairs is very slow. We examine the region of interest where one has an ensemble of overlapping instantons and bracket this regime with configuration ensembles having 20, 40 and 60 sweeps of smearing. Using the number of local maxima found in the action density, we find pseudoparticle densities of $7.9, 3.6$, and 2.4 fm^{-4} for 20, 40, and 60 sweep ensembles respectively.

B. Gell-Mann-Oakes-Renner Relation

We commence with an investigation of the pion mass and consider the standard pseudoscalar interpolating field $\chi = \bar{u}^a(x) \gamma_5 d^a(x)$. Our first consideration is the extent to which the Gell-Mann-Oakes-Renner [39] relationship between the squared pion mass and the quark mass ($m_u = m_d = m_q$)

$$m_\pi^2 = -\frac{2 \langle q\bar{q} \rangle}{f_\pi^2} m_q, \quad (14)$$

is maintained on the smeared ensembles. We consider a wide range of hopping parameter values, κ , and examine the relationship between the squared pion mass and $1/\kappa \propto m_q$.

Unlike the case of centre-vortex removal [40], we find a linear relationship at all levels of smearing. This enables the standard approach of dealing with the additive renormalisation of the quark mass in Wilson-like fermion formulations such as the FLIC fermion action considered herein. The critical value of the hopping parameter, κ_{cr} , where the pion mass vanishes is determined by linearly extrapolating m_π^2 as a function of $1/\kappa$ to zero. The additively renormalised quark mass is then provided by the standard relation

$$m_q = \frac{1}{2a} \left(\frac{1}{\kappa} - \frac{1}{\kappa_{\text{cr}}} \right). \quad (15)$$

The value of κ_{cr} observed depends significantly on the first few sweeps of smearing. Its deviation from the tree level value of $1/8$ is an indication of the additive renormalisation of the quark mass induced by the explicitly broken chiral symmetry of the Wilson action. As smearing removes the perturbative physics which acts to renormalise κ_{cr} away from its tree level value, one observes a return of κ_{cr} to 0.125. Similarly, the mean link, provided by the fourth root of the average plaquette, approaches 1. For example, after 10 sweeps of smearing, the original value of $\kappa_{\text{cr}} = 0.135$ becomes 0.126 and $u_0 = 0.86$ subsequently exceeds 0.995. The latter result indicates that the multiplicative renormalisation of the quark mass in the smeared ensembles is negligible.

Our results are illustrated in Fig. 4. The Goldstone nature of the pion is indeed retained. However there is a significant variation in the slope of the linear relation that reflects an important change in the manner in which the quark mass manifests itself in the interacting field theory.

The slope, $-2 \langle q\bar{q} \rangle / f_\pi^2$, can be regarded as an indicator of the level of instanton preservation under smearing. Figure 5 illustrates its evolution under smearing. In an instanton model, the quark condensate is proportional to \sqrt{n} , where n is the instanton density. Thus it is understandable that the slope reduces under smearing as instanton-anti-instanton pairs are annihilated.

In comparing results from different levels of smearing, one can choose to keep the bare mass, m_q , fixed, or keep m_π fixed as a measure of the renormalised quark mass. We choose the latter as providing the more physical relationship between ensembles with differing levels of smearing. It also enables a connection to the original unsmeared ensemble results.

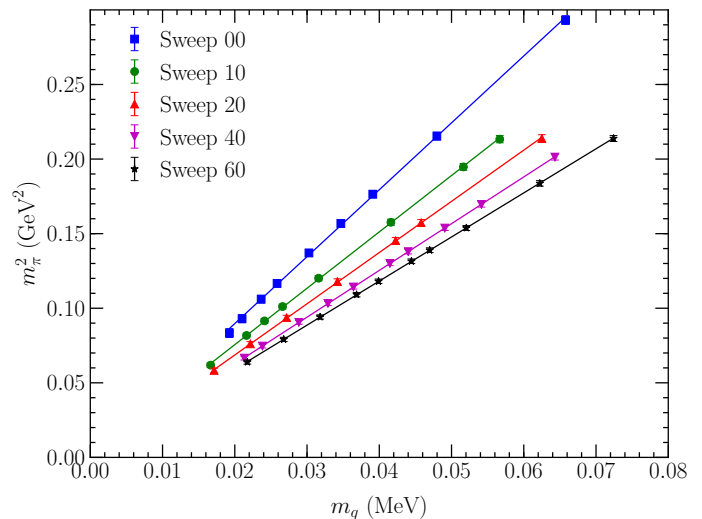


FIG. 4. The squared pion mass is plotted as a function of the Wilson quark mass of Eq. (15). Results are provided for the original configurations (Sweep 0) and for the ensembles following various levels of over-improved stout-link smearing as indicated.

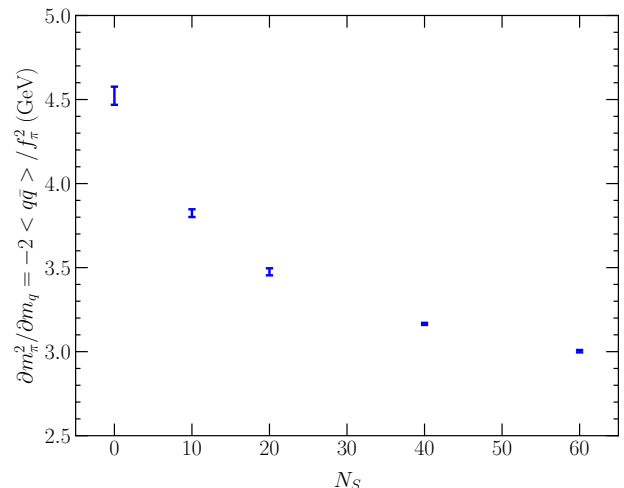


FIG. 5. The slope of the Gell-Mann-Oakes-Renner relation as a function of smearing.

C. Ground-state hadrons

We now consider the remaining lowest-lying light hadrons with non-vanishing masses in the chiral limit: the rho meson, the nucleon, and the Delta baryon. We use the standard interpolating fields for the ρ : $\bar{u}^a \gamma_\mu d^a$, nucleon: $\epsilon^{abc} (u^{Ta} C \gamma_5 d^b) u^c$, and Δ : $\epsilon^{abc} (u^{Ta} C \gamma_\mu u^b) u^c$, and construct a 4×4 correlation matrix. A combination of Gaussians with $N_{sm} = 25, 50, 100, 150$ was chosen to isolate states on the less-smeared configurations ($N_s < 40$). For the more heavily smeared configurations, the smoother background causes the process of source smearing to be more effi-

cient - the same number of smearing sweeps gives a larger source. Thus, the $N_{sm} = 100$ and $N_{sm} = 150$ sources became too similar in shape for any linear combination of them to resolve different states. Thus, for these configurations ($N_s = 40, N_s = 60$), the basis $N_{sm} = 10, 25, 50, 100$ was chosen.

As illustrated in Figs. 6 through 8, the hadron masses display a common trend of reduction as the underlying instanton content of the vacuum is eroded through pair annihilation under smearing. Only subtle changes in the pion mass dependence of the hadron masses are observed.

However, an important difference between these hadronic observables and gluonic observables is apparent. While gluonic observables such as the action, and the short-distance potential undergo rapid transitions during the first few sweeps of smearing, these hadronic observables display very little change over the first 10 sweeps. One can conclude that the rapid loss of action density in the first few sweeps of cooling is not connected to the low-lying hadron masses in a significant manner. Rather it is the loss of closely spaced instanton-anti-instanton pairs over more extensive smearing extents that gives rise to a loss of dynamical mass generation and lower lying hadron masses.

However, we emphasize the pion is different. At larger values of the quark mass, the pion mass displays a more rapid transition over the first few sweeps as reported in Fig. 4. This behaviour contrasts the ρ , N and Δ where the change in the hadron mass is relatively insensitive to the quark mass.

To perform a more quantitative examination of these hadron masses we interpolate the results to a common pion mass of 300 MeV and increase the statistical sample size by calculating 8 fermionic sources (shifting by a quarter of the temporal extent, and by half the spatial extent in each direction) per configuration for a total of 608. We also consider an interpolation to $m_\pi = 400$ MeV to expose any sensitivity to our selection of a comparison point. We note that for $m_\pi = 300$ MeV, $m_\pi L \sim 4$ such that finite-size effects are unlikely to affect the results in a significant manner.

Figures 9 and 10 report the results. While the hadron masses show a decline under smearing, we note that this decline is uniform for the N and Δ . The mass splitting $M_\Delta - M_N$ is invariant under smearing.

This invariance is interesting in the context of an instanton model where a strong attractive contribution to the nucleon mass originates from the interaction of the scalar diquark component with a single instanton or with a pair of an instanton and an anti-instanton (in the sum-rule context, the single-instanton contribution is necessary to stabilise the correlator) [10, 41, 42]. This contribution is necessarily large in typical models in order to replicate the observed nucleon-Delta mass splitting. In contrast, the lowest order contribution to the Delta requires twice as many zero-mode contributions and the instanton contribution to the mass is therefore higher order in n/V . In the current investigation, once the ultraviolet interactions have been suppressed under smearing, the main change to the gauge fields under further smearing is the annihilation of adjacent instanton-anti-instanton pairs. As the instanton-based model experiences a reduction in the scalar

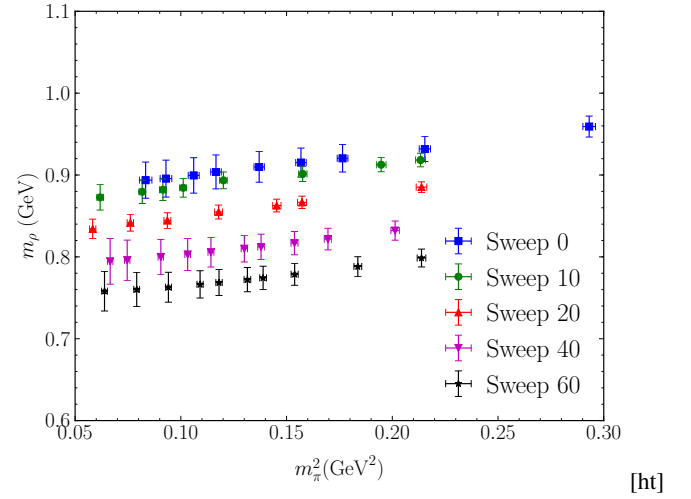


FIG. 6. Quark-mass dependence of the rho meson mass for various levels of smearing.

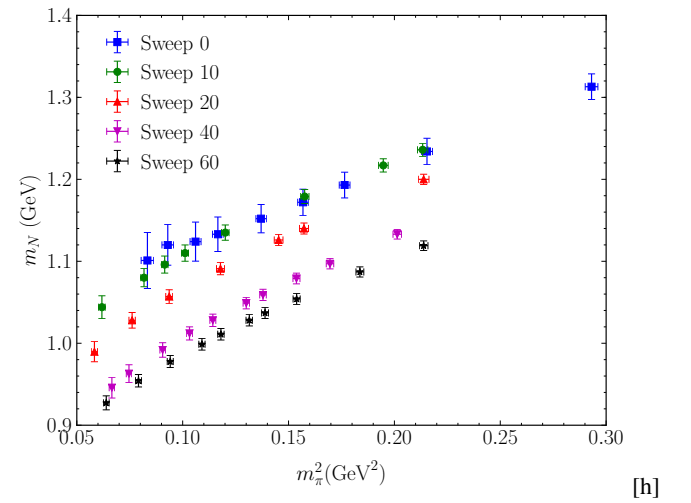


FIG. 7. Quark-mass dependence of the nucleon mass for various levels of smearing.

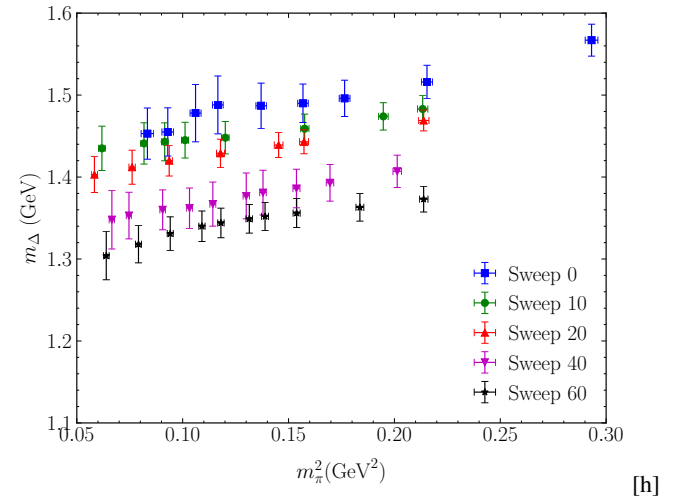


FIG. 8. Quark-mass dependence of the Δ mass for various levels of smearing.

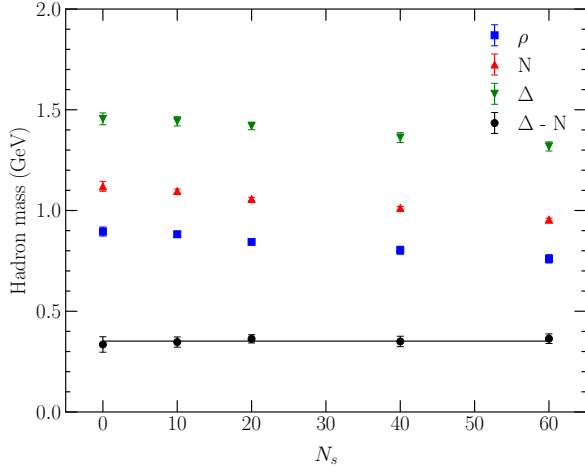


FIG. 9. Hadron masses, interpolated to a common pion mass of 300 MeV, are illustrated as a function of the number of smearing sweeps, N_s . The nucleon-Delta mass splitting, $M_\Delta - M_N$, is also illustrated. A fit of this splitting to a constant illustrates the invariance of the nucleon-Delta mass splitting to a thinning of the (anti-)instanton density.

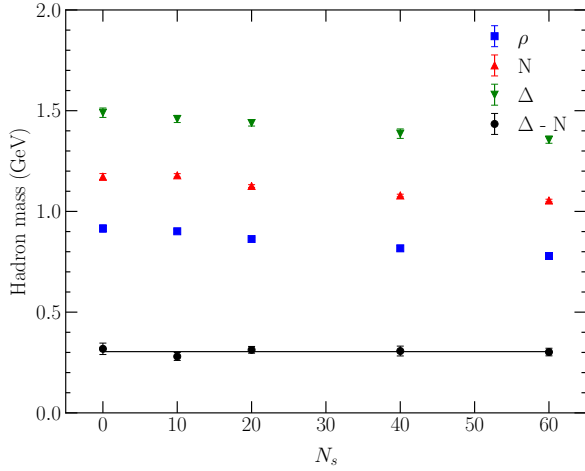


FIG. 10. Hadron masses, interpolated to a common pion mass of 400 MeV, are illustrated as a function of the number of smearing sweeps, N_s . A fit of the nucleon-Delta mass splitting, $M_\Delta - M_N$, to a constant illustrates the invariance of the nucleon-Delta mass splitting to a thinning of the (anti-)instanton density.

diquark attraction in the nucleon, it predicts a narrowing of the nucleon-Delta mass splitting under smearing. However, this is not observed. Figures 9 and 10 display a nucleon-Delta mass splitting that is invariant under smearing. Thus, the simple direct-instanton effect cannot be responsible for the lightness of the nucleon compared to the Delta.

In summary, the nucleon and Delta masses decrease under over-improved stout-link smearing. The reduction is the order of 10% of their original masses after 60 sweeps of smearing. However the mass splitting between them is insensitive to the loss of instanton pairs under smearing. Their mass splitting remains constant within error. The loss of instanton-induced

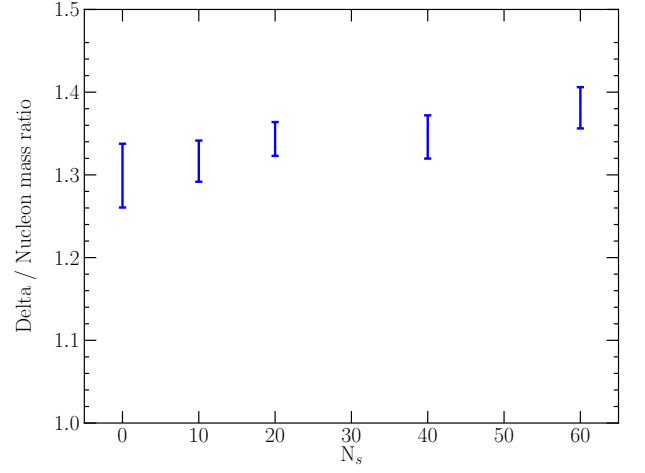


FIG. 11. The dependence of the Δ/N mass ratio evaluated at $m_\pi = 300$ MeV on the number of smearing sweeps. The ratio increases with smearing, reflecting a constant mass splitting in the context of decreasing baryon masses due to a thinning of the (anti-)instanton density.

scalar-diquark attraction in the nucleon predicted by the simple direct-instanton effect is not apparent. Although the majority of the hadron mass can be considered as generated by instanton interactions, this hadron-instanton interaction is not described using the 'tHooft interaction from a single instanton pair.

It is important to place this modern analysis in the context of an early analysis [25] that reported results consistent with the instanton model prediction. This early study considered smaller $16^3 \times 24$ lattices with an uncooled lattice spacing of 0.168 fm. The ensemble consisted only of 19 gauge configurations, and the hadron masses on the cooled ensembles were fitted using their dispersion relation because the statistical variation was too large on the cooled configurations to use the asymptotic behaviour of e^{-mt} . The associated large discretisation errors combined with unimproved cooling led to the rapid reduction of both ultraviolet physics and instanton content. Individual instantons are destroyed under unimproved cooling leading to a rapid loss of gauge field dynamics. Using the nucleon mass to reset the lattice spacing after cooling, the Delta was found to be “too light.” The present analysis suggests that this loss of mass splitting reflects a loss of gauge field dynamics such that the nucleon and Delta simply become degenerate. In other words, the dynamics responsible for splitting them has been destroyed under unimproved cooling.

In contrast, the invariant mass splitting observed in the present analysis occurs in the context of declining nucleon and Delta masses. As a result, the Delta-nucleon mass ratio actually increases under smearing as illustrated in Fig. 11. While good agreement with the physical ratio of 1.31 is observed at small numbers of smearing sweeps, the Delta is “too heavy” at 60 sweeps of smearing when measured relative to the nucleon mass.

D. Excited States

Our use of the correlation matrix method to cleanly isolate the lowest-lying states presented thus far has the additional advantage that we are able to examine the behaviour of excited states under smearing. To the best of our knowledge, this is the first examination of the role of instanton degrees of freedom in describing the radial excitations of hadrons.

Figures 12 through 14 illustrate the very different behaviour of hadronic excitations under smearing. The variation in mass is not at the level of the 10% observed for ground states, but is the order of 30%. Moreover, a significant mass drop is observed for as few as 10 sweeps of smearing, signaling an important role for ultraviolet physics.

We note that the excited states at 40 sweeps of smearing do not follow the monotonic trend set by the other smearing levels. We believe these energies are affected by near-by states that are not adequately accommodated in the 4×4 correlation matrix considered, giving rise to a superposition of excited states in the reported results. While we include them here for completeness, we will set them aside for the remainder of the discussion.

As for the ground states, we interpolate the hadron masses to a common pion mass of 300 and 400 MeV. Their dependence on the number of smearing sweeps is illustrated in Figs. 15 and 16. While the ground-state hadrons remained qualitatively unchanged under smearing, the excited states decrease in mass significantly. Continued smearing leads to a significant decline in the excitation energy, again emphasizing an important role for instanton degrees of freedom in generating the excitation spectrum.

An analysis of the associated eigenvectors for the excited states indicates that these states have the expected single-node structure in their wave function. The node is generated through a superposition of broad and narrow Gaussian smeared sources with opposite signs.

E. Non-relativistic Quark Model Consideration

An interesting question is the extent to which our results reported in Figs. 15 and 16 can be described by a simple constituent quark model, drawing on the change of the static quark potential examined in Fig. 2.

Here we consider the ρ meson. Using our fits to the static quark potential illustrated in Fig. 2, we solve the Schrödinger equation using a fixed constituent quark mass of 400 MeV and boundary conditions emulating the periodic lattice condition of the spatial volume.

As displayed in Fig. 17, this naive model predicts a much faster decrease in the ground-state mass than we observe in the lattice calculation. Moreover, the excited state mass is maintained better than the ground state under smearing. This qualitative difference allows us to conclude that a simple modification of the potential energy between constituent quarks is insufficient to capture the essence of the modification of the QCD vacuum under smearing.

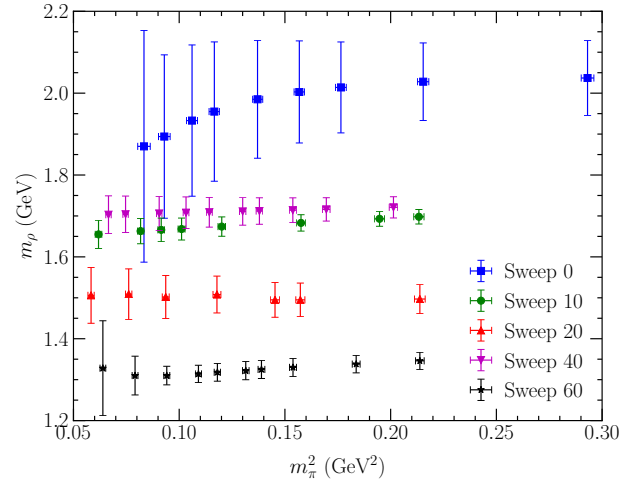


FIG. 12. Quark-mass dependence of the first excited-state energy of the rho meson observed in our correlation-matrix analysis for various levels of smearing.

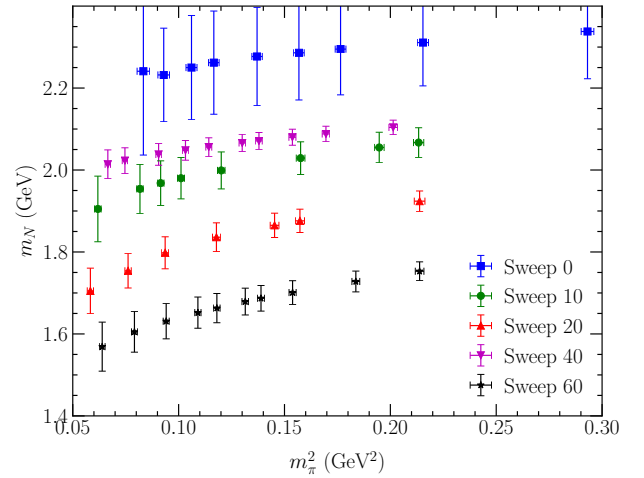


FIG. 13. Quark-mass dependence of the first excited-state energy of the nucleon observed in our correlation-matrix analysis for various levels of smearing.

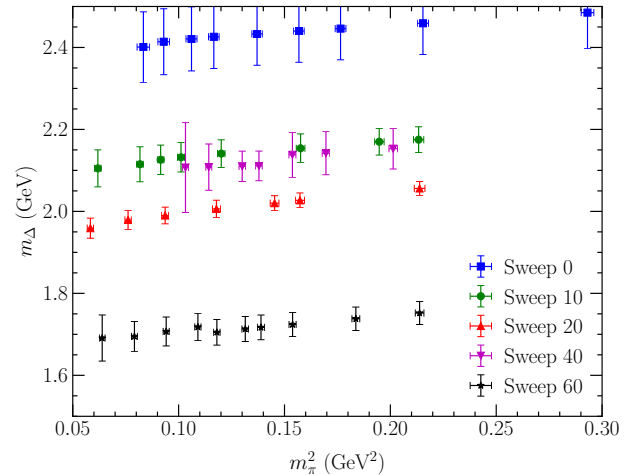


FIG. 14. Quark-mass dependence of the first excited-state energy of the Delta observed in our correlation-matrix analysis for various levels of smearing.

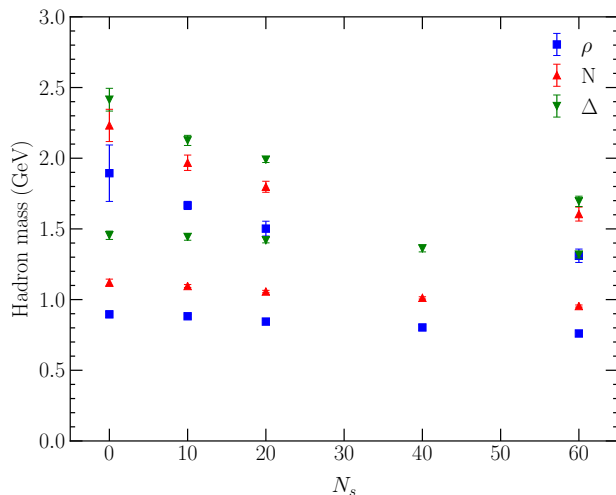


FIG. 15. The observed energies of the first excited states of our correlation matrix analysis are interpolated to a common pion mass of 300 MeV and plotted as a function of the number of smearing sweeps, N_s , to reveal the role of instanton degrees of freedom in generating the spectrum of excited states. The ground state masses are also replotted for comparison.

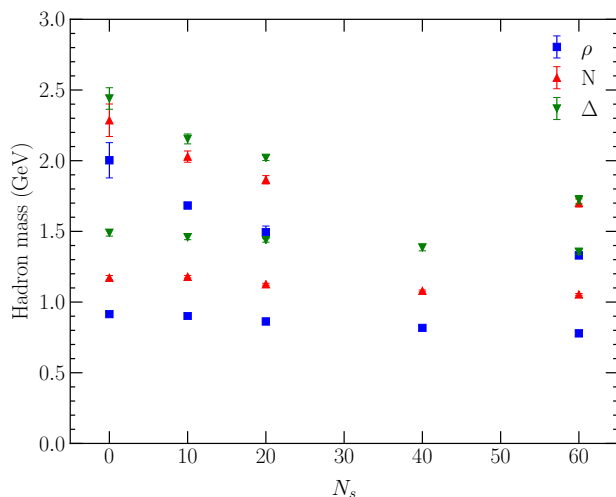


FIG. 16. The observed energies of the first excited states of our correlation matrix analysis are interpolated to a common pion mass of 400 MeV and plotted as a function of the number of smearing sweeps, N_s , to reveal the role of instanton degrees of freedom in generating the spectrum of excited states. Again, the ground state masses are shown for comparison.

V. CONCLUDING REMARKS

The light hadron spectrum has been examined in lattice QCD where the vacuum is altered using the over-improved stout-link smearing algorithm designed to retain separated instantons. The change in the ground-state hadron masses of the ρ , N and Δ is of the order of 10%, indicating that almost all

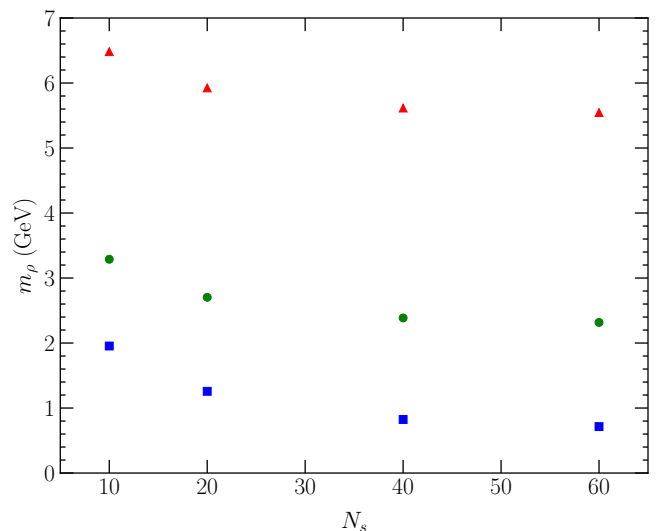


FIG. 17. Ground, first- and second-excited state masses of the ρ meson from a nonrelativistic quark-model calculation based on the static quark potential fits illustrated in Fig. 2. Masses may be shifted vertically by introducing a constant into the potential.

of the mass is generated by topological structures similar to instantons.

However, the difference between the Delta and nucleon masses is insensitive to smearing and the associated thinning of (anti-)instantons on the lattice. Even though the smearing process destroys topology by pairwise annihilation, the anticipated attractive contribution to the nucleon mass from the scalar-diquark direct-instanton interaction does not weaken during this process. This indicates that direct instanton-induced effects are not the dominant contribution to the hadronic masses.

Similarly, simple quark model phenomenology differs from the results observed on the lattice. A deeper understanding of the underlying mechanisms of QCD could be obtained through the operator product expansion of two-point hadron correlation functions. The evolution of vacuum condensates under smearing could be examined and the impact of this evolution on the spectral properties of the correlators could be studied. We will leave this study for a future investigation.

VI. ACKNOWLEDGEMENTS

It is a pleasure to acknowledge James Zanotti, Jon-Ivar Skullerud and Daniel Trewartha for interesting discussions. This research was undertaken on the NCI National Facility in Canberra, Australia, which is supported by the Australian Commonwealth Government. We also acknowledge eResearch SA for generous grants of supercomputing time. This research is supported by the Australian Research Council under grants DP1201104627 and DP15013164.

-
- [1] A. Belavin, A. Polyakov, A. Schwartz, and Y. Tyupkin, *Phys.Lett.* **B59**, 85 (1975).
 - [2] E. V. Shuryak, *Nucl.Phys.* **B203**, 93,116,140 (1982).
 - [3] E. V. Shuryak, *Nucl.Phys.* **B214**, 237 (1982).
 - [4] E. V. Shuryak, *Nucl.Phys.* **B302**, 559,574,599,621 (1988).
 - [5] E. V. Shuryak, *Nucl.Phys.* **B319**, 521,541 (1989).
 - [6] E. V. Shuryak, *Nucl.Phys.* **B328**, 85,102 (1989).
 - [7] I. Horvath *et al.*, *Phys.Rev.* **D66**, 034501 (2002), hep-lat/0201008.
 - [8] E. V. Shuryak and J. J. M. Verbaarschot, *Nucl.Phys.* **B410**, 37 (1993).
 - [9] E. V. Shuryak and J. J. M. Verbaarschot, *Nucl.Phys.* **B410**, 55 (1993).
 - [10] E. V. Shuryak and J. J. M. Verbaarschot, *Nucl.Phys.* **B412**, 143 (1994).
 - [11] T. Schäfer and E. V. Shuryak, *Rev. Mod. Phys.* **70**, 323 (1998).
 - [12] E. Shuryak, (2014), 1401.2032.
 - [13] P. J. Moran and D. B. Leinweber, *Phys.Rev.* **D77**, 094501 (2008), 0801.1165.
 - [14] M. G. Perez, A. Gonzalez-Arroyo, J. Snippe, and P. van Baal, *Nucl.Phys.* **B413**, 535 (1994).
 - [15] K. Symanzik, *Nucl.Phys.* **B226**, 187 (1983).
 - [16] C. Bonati and M. D’Elia, *Phys.Rev.* **D89**, 105005 (2014), 1401.2441.
 - [17] P. J. Moran and D. B. Leinweber, *Phys.Rev.* **D78**, 054506 (2008), 0801.2016.
 - [18] C. Michael, *Nucl.Phys.* **B259**, 58 (1985).
 - [19] M. Luscher and U. Wolff, *Nucl.Phys.* **B339**, 222 (1990).
 - [20] UKQCD Collaboration, C. McNeile and C. Michael, *Phys.Rev.* **D63**, 114503 (2001), hep-lat/0010019.
 - [21] M. S. Mahbub, W. Kamleh, D. B. Leinweber, P. J. Moran, and A. G. Williams, *Phys.Lett.* **B707**, 389 (2012), 1011.5724.
 - [22] M. S. Mahbub, W. Kamleh, D. B. Leinweber, P. J. Moran, and A. G. Williams, *Phys.Rev.* **D87**, 094506 (2013), 1302.2987.
 - [23] B. J. Owen *et al.*, *Phys.Lett.* **B723**, 217 (2013), 1212.4668.
 - [24] D. S. Roberts, W. Kamleh, and D. B. Leinweber, *Phys.Rev.* **D89**, 074501 (2014), 1311.6626.
 - [25] M. Chu, J. Grandy, S. Huang, and J. W. Negele, *Phys.Rev.* **D49**, 6039 (1994), hep-lat/9312071.
 - [26] T. Schäfer and E. V. Shuryak, *Phys.Rev.* **D50**, 478 (1994).
 - [27] J. W. Negele, (1997), hep-lat/9709129.
 - [28] T. DeGrand, A. Hasenfratz, and T. G. Kovcs, *Physics Letters B* **420**, 97 (1998).
 - [29] J. M. Zanotti *et al.*, *Phys.Rev.* **D65**, 074507 (2002), hep-lat/0110216.
 - [30] J. Zanotti, B. Lasscock, D. Leinweber, and A. Williams, *Phys.Rev.* **D71**, 034510 (2005), hep-lat/0405015.
 - [31] S. Boinepalli, W. Kamleh, D. B. Leinweber, A. G. Williams, and J. M. Zanotti, *Phys.Lett.* **B616**, 196 (2005), hep-lat/0405026.
 - [32] W. Kamleh, D. B. Leinweber, and A. G. Williams, *Phys.Rev.* **D70**, 014502 (2004), hep-lat/0403019.
 - [33] J. Zanotti, D. Leinweber, W. Melnitchouk, A. Williams, and J. Zhang, *Lect.Notes Phys.* **663**, 199 (2005), hep-lat/0407039.
 - [34] C. Morningstar and M. J. Peardon, *Phys.Rev.* **D69**, 054501 (2004), hep-lat/0311018.
 - [35] S. Gusken, *Nucl.Phys.Proc.Suppl.* **17**, 361 (1990).
 - [36] R. Brower, D. Chen, J. Negele, and E. Shuryak, *Nuclear Physics B - Proceedings Supplements* **73**, 512 (1999).
 - [37] A. S. Bakry, D. B. Leinweber, and A. G. Williams, *PoS LAT-TICE2011*, 256 (2011), 1107.0150.
 - [38] D. Trewartha, W. Kamleh, D. Leinweber, and D. S. Roberts, *Phys.Rev.* **D88**, 034501 (2013), 1306.3283.
 - [39] M. Gell-Mann, R. J. Oakes, and B. Renner, *Phys.Rev.* **175**, 2195 (1968).
 - [40] E.-A. O’Malley, W. Kamleh, D. Leinweber, and P. Moran, *Phys.Rev.* **D86**, 054503 (2012), 1112.2490.
 - [41] A. Dorokhov and N. Kochelev, *Zeitschrift für Physik C Particles and Fields* **46**, 281 (1990).
 - [42] H. Forkel and M. K. Banerjee, *Phys. Rev. Lett.* **71**, 484 (1993).